Electrical Supplementary Information

Empowering Microfluidics by Micro-3D Printing and Solution-based Mineral Coating

Hongxia Li, Aikifa Raza, Qiaoyu Ge, Jin-You Lu, TieJun Zhang*

Department of Mechanical Engineering, Masdar Institute,
Khalifa University of Science and Technology, P.O. Box 54224, Abu Dhabi, UAE.

*Correspondence and requests for materials should be addressed to T.J. Zhang
(email: tiejun.zhang@ku.ac.ae)

S1. Stability of Seed/Ionic Solutions

The stability of the seed solution is shown in **Figure** S1a. Because spontaneous aggregation may occur, the solution must be prepared right before the injection. In **Figure** S1b, we measured the pH value of the Ca^{2+}, CO_3^{2-} ionic solution. At the first 30 minutes, the solution was kept under room temperature and it was very stable as reflected by constant pH value. At t=30 min, the solution was placed into the 40 °C water bath. A continuous decrease of pH value was observed. That is because the solution becomes supersaturated at the elevated temperature. Consequently, the crystals started to form and precipitate on the beaker surfaces (the inset image of **Figure** S1b).

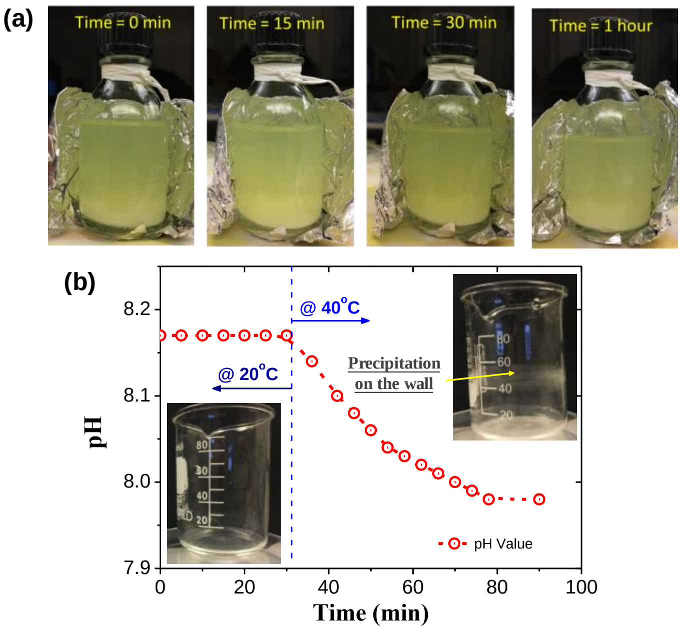

Figure S1. Stability of coating solutions.

S2. Fluid Injection Experimental Setup and Coating Procedure

Figure S2 shows the step-by-step procedures of internal solution-based coating in 3D-printed micromodel. A micro-scale flooding system as shown in **Figure** S2d was built. The pressure controller is used to control the flow rate or the injection pressure during the flooding experiment. It pumps N_2 gas into the reservoir bottle so that the pressurized liquid then enters the microfluidic models. According to the experimental needs, different fluids such as seed/ionic solution are contained in the reservoir bottles. During the flooding process, the flow rate and pressure can be monitored by the volumetric flow meter and pressure sensor, respectively.

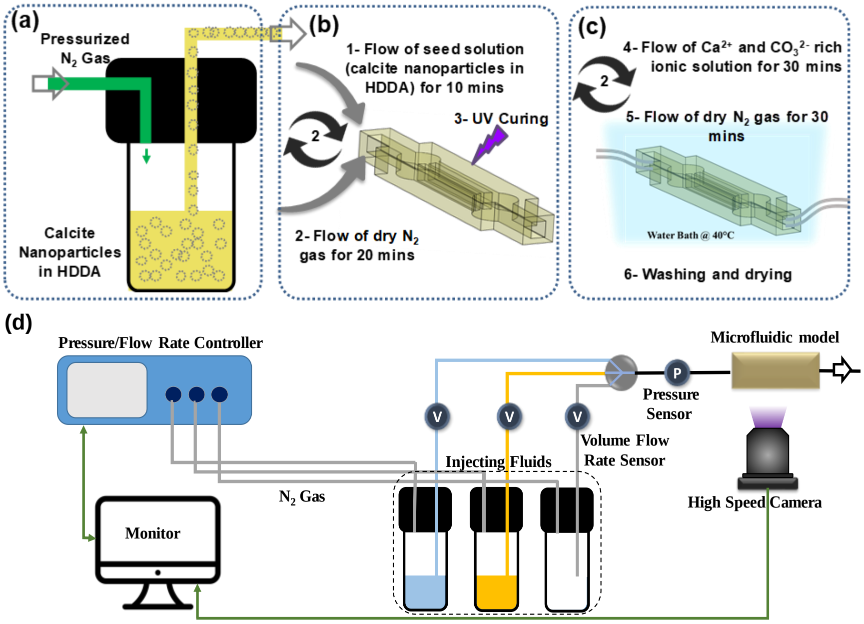

Figure S2. Step-by-step calcite coating in micromodel: (a, b) Injection of seed solution into the as-printed 3D micromodel to form a thin liquid film along the inner surfaces, followed by photopolymerization; (c) injection of supersaturated ionic solution into the 3D micromodel. (d) The fluid injection setup.

S3. Light Scattering and Transmission Loss of Particles-Added Ink

Adding CalNPs into the monomer ink can cause severe light scattering. To check the light-ink interaction, Finite-Difference Time-Domain (FDTD) optical simulation is conducted on a 10 μm × 10 μm × 15 μm cube with the ink with randomly distributed calcite NPs. A Gaussian light illumination with wavelength 408 nm is employed at plane Z=0. Along with the light penetration into the ink, its intensity distribution on the XZ plane is given in **Figure** S3a. In the pure ink without any NPs, the light intensity is maintained as a smooth Gaussian distribution when the light penetrates into the ink. However, the light intensity distribution becomes sparkling inside the NPs-added ink. By comparing the last three images in **Figure** S3a, we find that the increase of NPs concentrations intensifies the light scattering effect. From **Figure** S3b, the fluctuations on the light intensity curves also show the light scattering in the NPs-added ink under various concentrations. For the interest, we also studied the effect of nanoparticle's refractive index on the light scattering. So, besides the calcite nanoparticles (relatively low refractive index, 1.63), we also tested a high-refractive-index material, i.e. SiC (2.67). In **Figure** S3c, the light can penetrate into particle-free ink as deep as 15 µm without changing its pattern. However, in the polymer/particle composites, the light pattern can only maintain within a 10 µm's penetration distance for low-refractive-index material and completely loses its shape after a 4µm's penetration distance for high-refractive-index material. In other word, to guarantee the printed geometry accuracy, we should be careful in controlling the layer thickness during the printing.

We also did the printing assessment with the above NPs-added solutions to check the feature accuracy. In the printing experiments, a mesh pattern is printed. As shown in the first image of **Figure** S3d, a very clear and sharp boundary is observed under the optical microscope when there is no NPs added into the ink. However, after adding NPs, a fuzzy boundary (indicating the roughness along the sidewalls) becomes visible as shown in the last three images. The roughness is more severe when we increase the NPs concentration. Both the simulation and experimental results extensively evidences that adding NPs deteriorate the performance of micro-3D printing.

Another concern of adding CalNPs into monomer ink is the transparency loss of as-printed micromodels. One of the key applications of microfluidic models is for flow imaging, so optical transparency of the micromodel is essential. **Figure** S3e shows the light transmission spectra of 40-µm thick polymeric films as printed with HDDA monomer ink with/without CalNPs, and their transmission losses after calcite coating. The transmission spectra were as recorded from 400 nm to 800 nm, corresponding to the light wavelength range of a halogen lamp, which is commonly used as the light source in the optical microscope for flow observation. As shown in **Figure** S3e, after adding CalNPs into monomer ink (CalNPs composite), the light transmission of as-printed film reduces to 30% (from the blue curve to the red curve). After calcite coating, the light transparency decreases further. However, the advantage of printing pure ink with subsequent calcite coating (blue circles) is still dominant in comparison with direct printing of CalNPs-added composite (red circles).

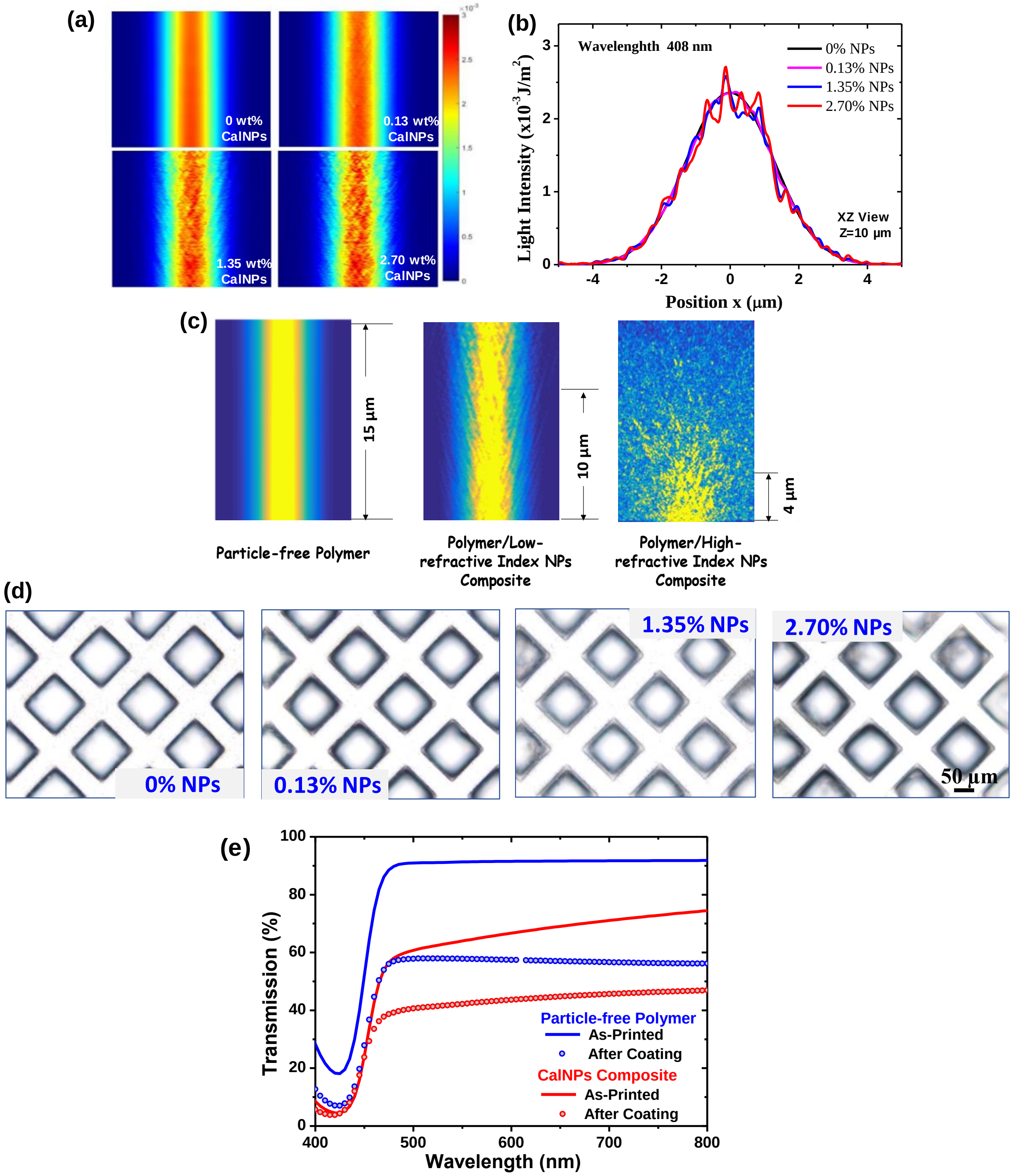

Figure S3. Light-ink interactions of polymer/particle composite and their impact on printing precision**.** (a, b) Effect of CalNPs concentration: (a) light intensity profile change along with its penetration into the printing ink and (b) fluctuations on the light intensity obtained from FDTD optical simulation. (c) Effect of nanoparticle's refractive index. (d) Mesh pattern printed with polymer/particle composites. (e) The transmission spectra of 40-μm thick flat films printed with particle-free ink and CalNPs composite as well as their transmission losses after calcite coating.

S4. Surface Morphology Before/After Coating

Figure S4 shows the AFM scan of CalNPs coated surface before and after water flush experiments. In the height profile image, the bright spots are the CalNPs. This is also confirmed by the stiffness profile in Figure 3a in the main manuscript, where the stiffness is found higher at the same place. By comparing the images before and after water flush, we found that most of the CalNPs stayed at the surfaces (the black spots are the missed nanoparticles after water flush). The strong stability is owing to the capillary-enhanced CalNPs immobilization as discussed in the main manuscript.

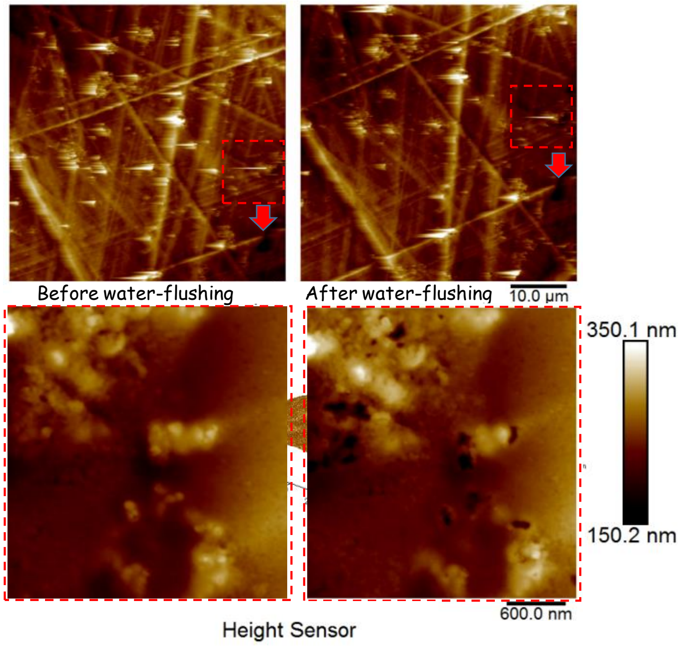

Figure S4. AFM scan of CalNPs coated surface before and after water flush.

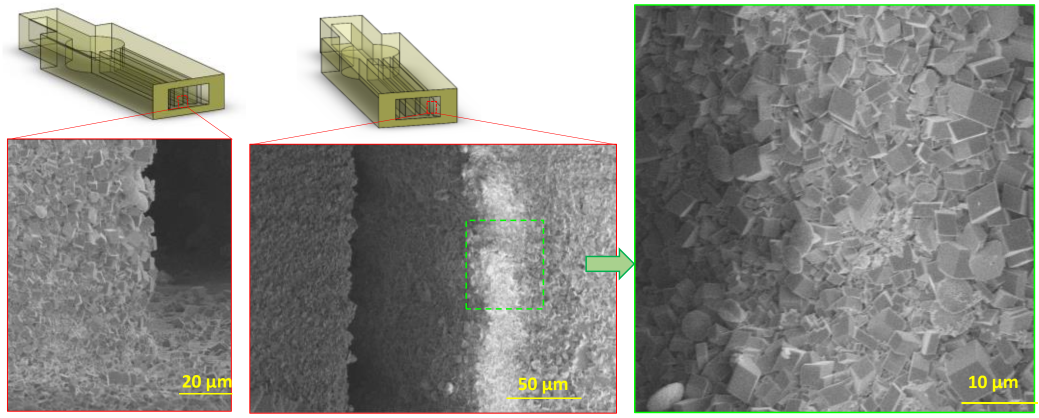

Figure S5. Surface morphology inside microchannels after coating. The SEM images are captured from different locations of the same micromodel in corresponding to Figure 5 in the main manuscript.

From the optical (**Figure** S6a) and SEM images (**Figure** S6b) of rock patterns before and after coating, we can find that only a thin layer of crystals is formed on the surfaces without considerably changing the pattern shape. Even inside the microchannels, the calcite crystals are very dense and uniformly distributed on the inner surfaces (see **Figure** S5).

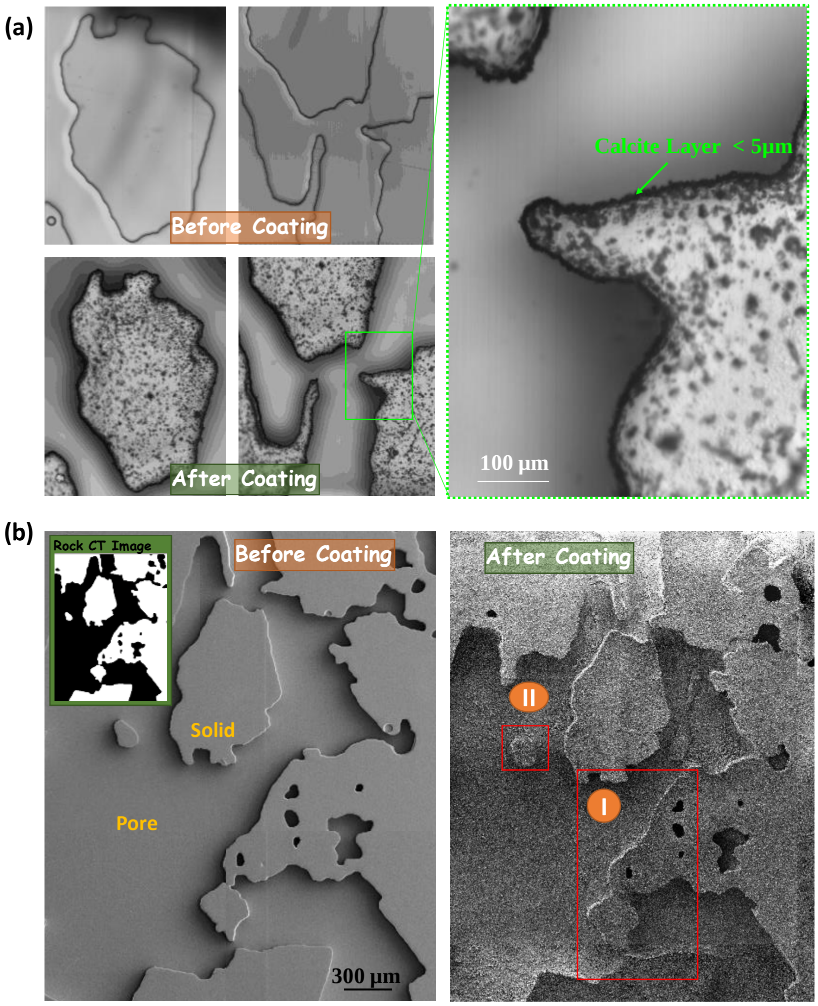

Figure S6. Surface morphology of rock micromodel before/after calcite coating: **o**ptical (a) and SEM (b) images.

S5. Surface Characterization under Different Growth Time

To have an idea of how the surface change during the calcite growing process, the SEM images showing surface morphology change and the contact angle showing surface wettability change are provided in **Figure** S7 and **Figure** S8.

Firstly, we printed some flat polymeric sheet from the same monomer ink (HDDA). After seeding CalNPs (~ 140 nm) on their surface, the HDDA surfaces were partially covered by the particles as shown in **Figure** S7. As a result, the water contact angle becomes 71° from 88° of the intrinsic HDDA surface as plotted in **Figure** S8, where we also provided the values of advancing and receding contact angle, which is also known as contact angle hysteresis.

After placing the sample in supersaturated Ca^{2+} CO_3^{2-} solutions for 0.5 hours, the crystals became visible on the surfaces. The crystal size is less than 1 μm. Meanwhile, some bared HDDA surfaces are also observed. Continuing the growth for another half hour, the crystal size increases into few microns, and the bare HDDA surfaces are no longer visible under the SEM. After 2 hours' growth, a very dense layer of calcite crystals is observed. The crystal sizes are ranging from sub-micron to few microns.

The surface wettability after different growth time can be seen from **Figure** S8. The water contact angle decreases gradually with the growth time. After 1 hour's growth, through the water droplet can form on the surface with a contact angle of 44 °, the receding contact angle became zero. After 2 hours' growth, the surface became totally water wet.

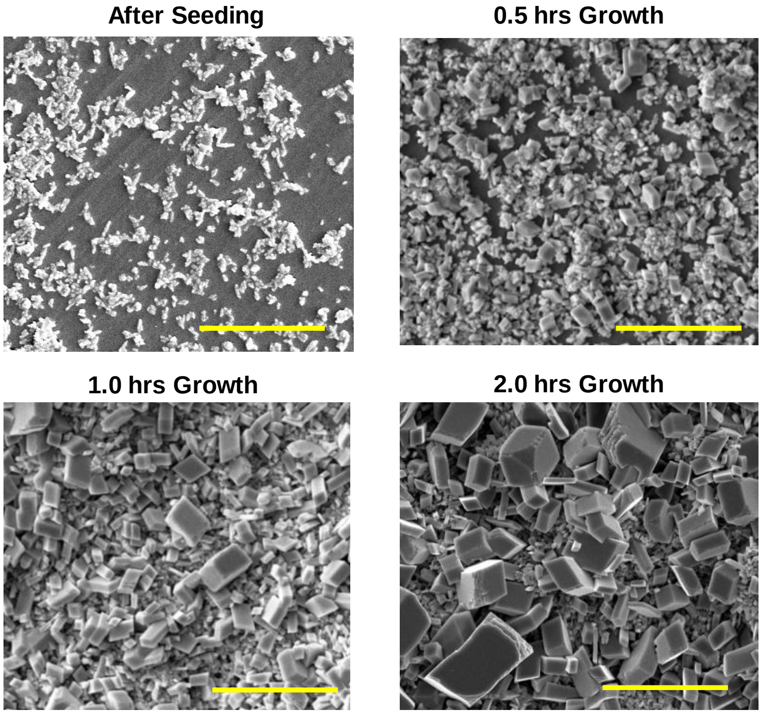

Figure S7. The change of crystal size with growing time. The scale bar for all the images is 5μm.

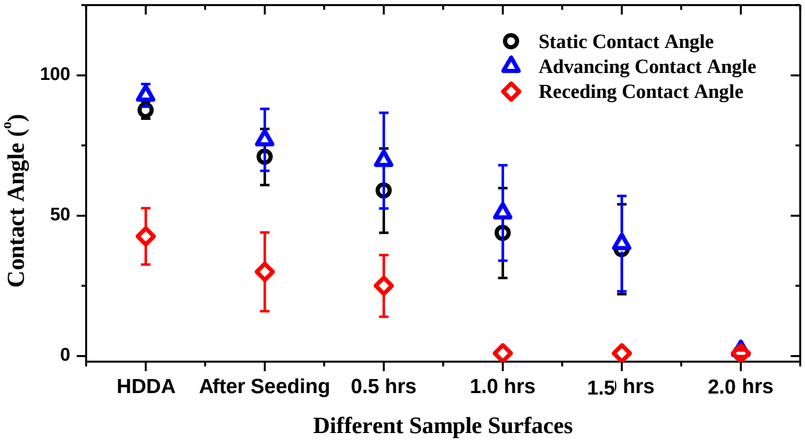

Figure S8. Contact angle change with growing time.

S6. Stress-strain analysis for polymer and its nanoparticle composite

We conducted the stress-strain analysis for pure polymer and polymer composite as shown in Figure S9. The thin strips of pure polymer ① and polymer composite ④ were fabricated in a UV chamber, while the strips ② ③ were fabricated by sequentially solidifying pure polymer segment (yellow) and CalNPs composite segment (brown). In comparison, the pure polymer has the highest Young's modulus around 3.84MPa. After adding CalNPs, the composite becomes slightly elastic (Young's modulus 2.06 MPa) but fragile. When stretching the combination strip, the break point was found in the composite part as shown in Figure 3 of the main manuscript.

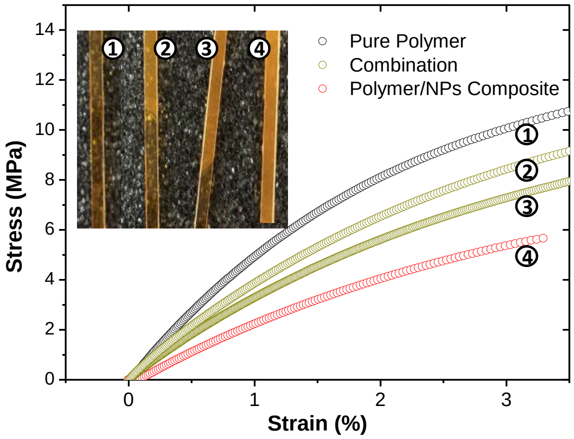

Figure S9. The strain-stress analysis for the polymer and its composite.